IOP Publishing 2D Mater. 8 (2021) 045024 https://doi.org/10.1088/2053-1583/ac10f1

2D Materials

RECEIVED
22 March 2021

ACCEPTED FOR PUBLICATION
1 July 2021

PUBLISHED
14 September 2021

PAPER

Application-driven synthesis and characterization of hexagonal boron nitride deposited on metals and carbon nanotubes

Victoria Chen[1], Yong Cheol Shin[1], Evgeny Mikheev[2,3], Qing Lin[4], Joel Martis[5], Ze Zhang[5], Sukti Chatterjee[6], Arun Majumdar[5,7], H-S Philip Wong[1], David Goldhaber-Gordon[2,3] and Eric Pop[1,7,*]

[1] Department of Electrical Engineering, Stanford University, Stanford, CA 94305, United States of America
[2] Department of Physics, Stanford University, Stanford, CA 94305, United States of America
[3] Stanford Institute for Materials and Energy Sciences, SLAC Natl. Accelerator Lab, Menlo Park, CA United States of America
[4] Department of Materials Science and Engineering, Stanford University, Stanford, CA 94305, United States of America
[5] Department of Mechanical Engineering, Stanford University, Stanford, CA 94305, United States of America
[6] Applied Materials, Inc., Santa Clara, CA 95054, United States of America
[7] Stanford Precourt Institute for Energy, Stanford, CA 94305, United States of America
[*] Author to whom any correspondence should be addressed.

E-mail: epop@stanford.edu

Keywords: hexagonal boron nitride (h-BN), 2D materials, CVD growth, carbon nanotubes (CNTs)

Supplementary material for this article is available online

Abstract

Hexagonal boron nitride (h-BN) is unique among two-dimensional materials, with a large band gap (∼6 eV) and high in-plane thermal conductivity (>400 W m^{-1} K^{-1}), second only to diamond among electrical insulators. Many studies to date have relied on exfoliated h-BN, however, for large-scale applications the material must be synthesized by methods such as chemical vapor deposition (CVD). Here, we first investigate single-layer h-BN synthesized by CVD on single crystal platinum (Pt), comparing these films with h-BN deposited on more commonly used polycrystalline Pt and Cu. The h-BN film grown on single crystal Pt has the lowest surface roughness and best spatial homogeneity, and our electrochemical transfer process allows the Pt to be reused with no measurable degradation. We also demonstrate direct capping of carbon nanotubes (CNTs) with as-grown h-BN, but we find that the direct growth partly degrades the CNT electrical conductivity. On the other hand, we show that transferred monolayer h-BN can serve as an ultrathin barrier which protects MoS_2 from damage at high temperatures and discuss other applications that take advantage of the conformal h-BN deposition.

1. Introduction

The family of two-dimensional (2D), layered materials are characterized by relatively strong in-plane bonds and weaker out-of-plane van der Waals coupling between layers. While there has been significant interest in the electrically conductive graphene and semiconducting transition metal dichalcogenides, there are also numerous applications for an electrically insulating 2D material. Hexagonal boron nitride (h-BN) in its monolayer form has a 'thickness' of 3.33 Å, taken as the interlayer spacing of the bulk material [1]. With an electrical band gap of 6 eV, h-BN is an electrical insulator structurally similar to graphene, but composed of ionically bonded boron and nitrogen atoms [2, 3]. This structure, which contains no out-of-plane dangling bonds, results in the h-BN film's high mechanical strength, chemical inertness, and extremely high in-plane thermal conductivity— greater than the thermal conductivity of bulk copper near room temperature [4–10].

The unique characteristics of h-BN have made it demonstratively useful as the gate dielectric in 2D field effect transistor [11], substrate and encapsulant for record high velocity saturation in graphene [12], passivation layer to protect air-sensitive materials as well as prevent electromigration [13, 14], and substrate for heat spreading [15]. While mechanical exfoliation from a bulk crystal can yield micron-sized h-BN flakes for proof-of-concept experiments, large area, continuous h-BN films are necessary for practical applications. A promising method to

© 2021 IOP Publishing Ltd

achieve this goal is through low-pressure chemical vapor deposition (LPCVD) at temperatures >900 °C [4, 16–18]. Monolayer and multilayer h-BN films have been grown on a variety of substrates, including metals such as copper, platinum, and nickel, and work is also being done in order to improve the scalability of these processes [18–22]. In addition, h-BN can be deposited on silicon-based substrates (SiO_2 and Si_3N_4) although the resultant film grain size is limited to ∼10–20 μm [23, 24], and by low-temperature electron-enhanced atomic layer deposition in nanocrystalline form [25]. These studies have demonstrated that the substrate material and crystallinity influence h-BN growth rates, spatial uniformity, and film quality. Researchers have also reported differences in h-BN film properties among different grains of the same growth substrate, another important factor to consider when targeting a uniform, high-quality film for several applications [16, 26].

However, despite growing interest in this material, a direct comparison of monolayer h-BN grown by CVD from an air-stable, solid-source precursor on polycrystalline Pt and single crystal Pt using the same deposition conditions has not been previously reported. Because Pt is a frequently used growth substrate, it is vital to understand the differences in film properties from different Pt crystallinities. Additionally, the characterization of h-BN deposited directly onto both single crystal Pt as well as other unconventional substrates (e.g. carbon nanotubes, CNTs) is relatively limited, even though direct deposition onto CNTs could enable improved device performance as gate dielectrics and CNT protection without requiring the transfer of h-BN. An in-depth study of CVD h-BN on a number of substrates can open doors to a variety of potential applications with unique requirements for the film properties.

Here we report the LPCVD of monolayer h-BN films on single crystal and polycrystalline Pt substrates, as well as multilayer h-BN films on both polycrystalline Cu foil and aligned, single-walled CNTs. From the metal growth substrates, the h-BN films are transferred off and characterized using atomic force microscopy (AFM) and Raman spectroscopy, yielding new data that illustrate h-BN film characteristic variations between h-BN from polycrystalline Pt vs. single crystal Pt. We additionally show cross-sectional transmission electron microscopy (TEM) images of the crystalline multilayer h-BN films from the Cu substrate and CNTs. Only one previous study [27] has experimentally shown CNTs wrapped with few-layer h-BN; going beyond this, here we provide the first demonstration of CNTs capped with as-grown h-BN, and their electrical characterization. We also demonstrate, for the first time, the use of monolayer h-BN as an ultrathin capping layer that protects monolayer MoS_2 from degradation in high temperature conditions.

2. Methods

Large-area (on the order of cm^2) h-BN films were prepared by LPCVD in a 50 mm diameter furnace that is schematically represented in figure 1(a). The Pt growth substrates (polycrystalline and single crystal) are placed on a quartz boat inside the furnace chamber and heated to 1100 °C, the Cu substrate to 1050 °C, and the CNTs on a quartz substrate to 1100 °C. In each case, the air-stable, solid source precursor, ammonia borane (H_3NBH_3), is placed in an ampoule that is heated independently from the main furnace chamber. The ammonia borane is heated to 100 °C, at which point it decomposes into borazine [$(HBNH)_3$], polyiminoborane (BHNH), and hydrogen [28]. H_2 is used as the carrier gas for the borazine to diffuse through the furnace, which is at ∼900 mTorr, and onto the growth substrates. The metal substrates were annealed at their respective growth temperatures for 40 min prior to the h-BN growth, which serves to remove impurities and, in the case of Cu, smooth the substrate surface. The substrates and relative thicknesses of h-BN deposited are schematically summarized in figures 1(b)–(e).

After completing the h-BN growths, we used an electrochemical bubbling method at room temperature to delaminate the h-BN films from the Pt substrates [18], and a wet etching method to transfer them from the Cu substrate to SiO_2. A more detailed discussion of the transfer process is included in supplementary information figure S1 (available online at stacks.iop.org/2DM/8/045024/mmedia). This process allows the expensive Pt substrates to be reused for hundreds of growths with no measurable degradation in the substrates or in the grown h-BN quality. Simultaneously, by utilizing this low-temperature transfer process, the h-BN film can ultimately be deposited onto another substrate that is never exposed to the high-temperature growth conditions. Therefore, this process is compatible with applications which contain temperature-sensitive substrates. The majority of samples in this work were transferred onto a 300 nm SiO_2 on Si substrate for characterization purposes. Transferring the h-BN films onto the same kind of substrates using the same transfer procedure ensures a fair comparison between films that were originally grown on different substrates.

While the large band gap of h-BN renders it almost optically transparent, especially for such thin films, we are able to see some optical contrast on the 300 nm SiO_2/Si substrates. The presence of h-BN is additionally verified using Raman spectroscopy, with a 532 nm laser and 100× objective. Bulk h-BN has a Raman peak centered at approximately 1366 cm^{-1}. However, thinner h-BN films exhibit blue shifts up to ∼4 cm^{-1} with monolayer samples having a peak centered at approximately 1370 cm^{-1} [29]. While this is commonly referred to as the E_{2g} peak, monolayer h-BN belongs to the D_{3h} point group, which differs

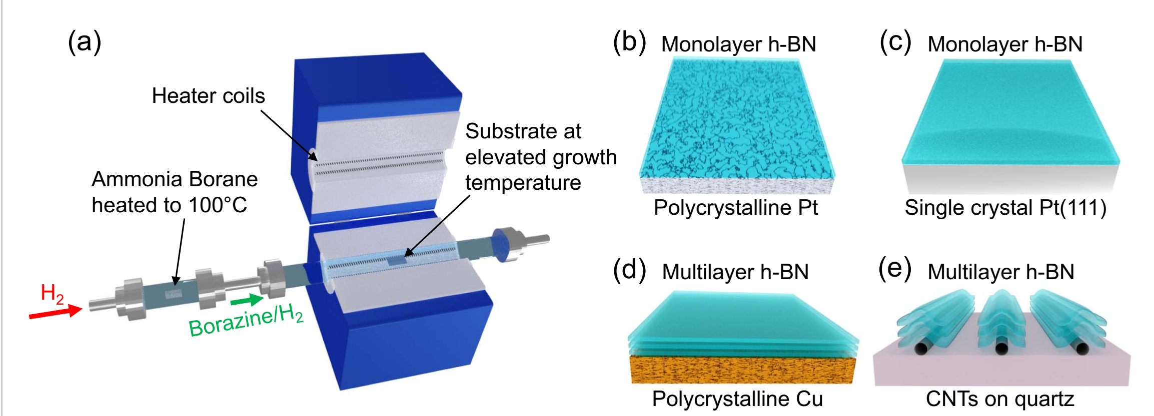

Figure 1. Schematics of the CVD furnace and growth substrates. (a) The CVD system used for h-BN growth, (b) monolayer h-BN on a polycrystalline Pt substrate, (c) monolayer h-BN on a single crystal Pt(111) substrate, (d) multilayer h-BN on a Cu substrate, and (e) multilayer h-BN on carbon nanotubes (CNTs) on a quartz substrate.

from the bulk point group (D_{6h}). Therefore, we refer to this peak at ~1370 cm^{-1} as the E′ peak [1, 41]. In monolayers, the E′ peak can shift because of the slightly shorter B–N bonds resulting from the missing interlayer forces that would lengthen B–N bonds in multilayer h-BN [30]. To characterize film thicknesses and compare surface roughness, we use AFM in non-contact mode with a scan rate of 0.5 Hz. We use scanning electron microscopy (SEM) as well as electron backscatter diffraction (EBSD) with an accelerating voltage of 20 kV to examine and analyze the crystallinity of the metal growth substrates. Finally, the samples for cross-sectional TEM imaging were capped with a protective carbon layer and cut with a focused ion beam.

3. Experimental results and discussion

The monolayer h-BN growth on Pt substrates is hypothesized to occur by physisorption after the thermal decomposition of the borazine [31]. After the initial monolayer is formed on these surfaces, the surface reactivity decreases and therefore the formation of additional h-BN layers slows, so that the CVD process on Pt is effectively limited to one monolayer at the growth pressure of ~900 mTorr, without the presence of bilayer regions [32]. On the other hand, it should be noted that other works report few-layer regions of h-BN deposited on polycrystalline Pt with different CVD conditions [26, 33]. Therefore, it is evident that the growth mechanisms are highly dependent on variables such as the precursor temperature and pressure of the furnace chamber.

Figure 2 compares the polycrystalline Pt with the single crystal Pt(111) substrate. Figure 2(a) shows a magnified optical image of the polycrystalline Pt foil, with an inset of a photograph of the substrate. Grains on the order of a few hundred μm appear as ‘sparkles’ to the naked eye due to different crystal orientations of the grains reflecting light differently. These grains are also shown by SEM in figure 2(b) and EBSD in figure 2(c). The boundaries between different Pt crystal orientations are very clear in the SEM and EBSD images, and these relatively sharp boundaries indicate that the grain size of the Pt substrate may be a limiting factor in the grain size of the h-BN that is grown. This hypothesis is further discussed in the supplementary information figure S2, which maps the spatial orientation of a monolayer h-BN film that was grown on polycrystalline Pt, revealing clusters of points with the same h-BN orientation in regions of comparable areas to the polycrystalline Pt grain size. Additionally, in supplementary information figure S3, we show an AFM topography scan over a grain boundary in the polycrystalline Pt. This image provides evidence of the thermal grooving that occurs in part due to the high temperature and low pressure of the CVD process, and this phenomenon is important to be aware of for scalable applications where a spatially uniform film is required [34].

Figure 2(d) shows an optical image of the single crystal Pt(111) substrate, with no grain boundaries visible optically or by the SEM image in figure 2(e). EBSD in figure 2(f) confirms the crystallinity. The surface of the Pt(111) substrate is smoother than the polycrystalline substrate and may demonstrate higher catalytic activity because of its relatively higher surface density of atoms (as compared to other crystal orientations). After characterizing the two Pt substrates, the same conditions (temperature, gas flow, and pressure) are used for CVD of h-BN growth on each. These h-BN films are then transferred with the same method onto 300 nm SiO_2 on Si substrates for further characterization.

In figure 3, we compare monolayer h-BN after transfer from the polycrystalline and Pt(111) substrates to the SiO_2/Si substrate. The bubbling-based transfer method has been demonstrated previously in the literature and is summarized in supplementary information figure S1 [18, 35]. Figures 3(a)–(c) show optical, Raman, and AFM images of the h-BN film transferred from the polycrystalline Pt substrate.

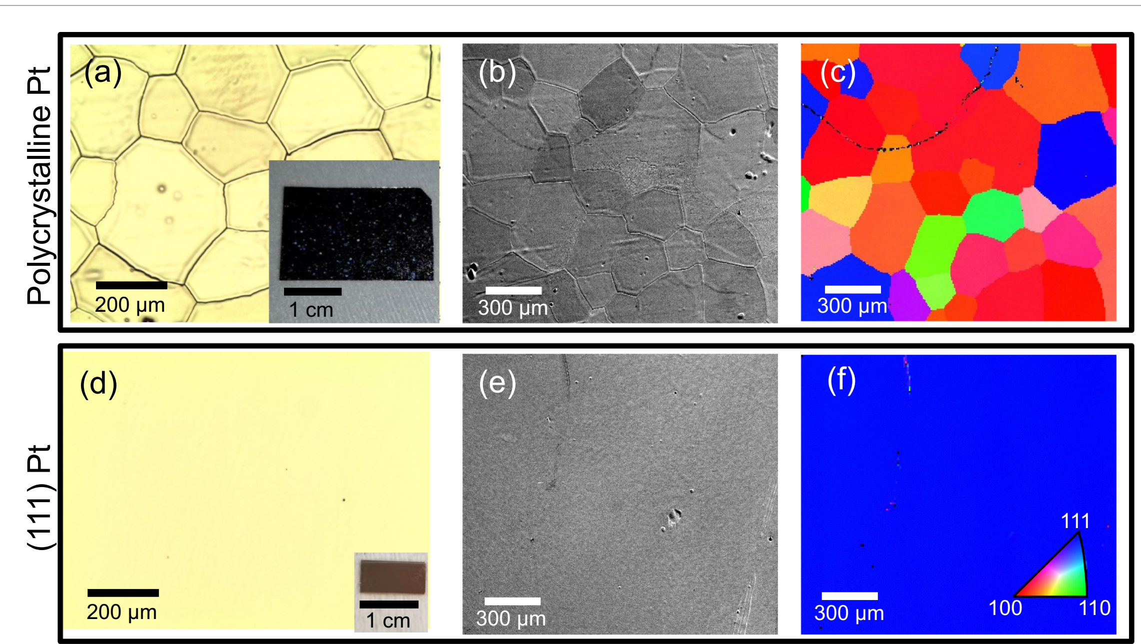

Figure 2. Imaging and characterization of Pt growth substrates for h-BN. (a) Zoomed-in optical image of polycrystalline Pt (inset zoomed-out, showing entire foil), (b) scanning electron microscope (SEM) image and (c) EBSD of the same polycrystalline Pt, showing the individual grains and grain boundaries. (d) Zoomed-in optical image of single crystal Pt(111) growth substrate (inset zoomed-out, showing entire sample), (e) SEM image and (f) EBSD of the same single-crystal Pt substrate.

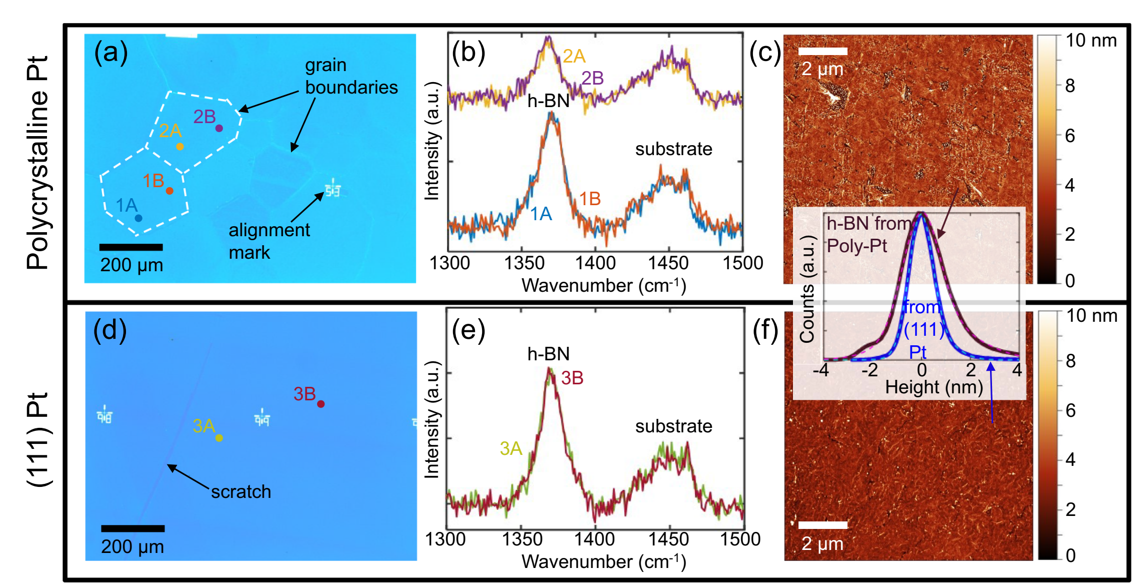

Figure 3. Characterization of grown h-BN transferred to SiO_2, from growth on (a)–(c) polycrystalline Pt foil and (d)–(f) on single-crystal Pt. (a) Optical image, (b) Raman spectra, and (c) AFM topography of h-BN from within a grain marked in (a). Raman signatures are the same within the same grain, but differ between grains. (Spectra offset for clarity.) (d) Optical image, (e) Raman spectra, and (f) AFM topography of h-BN grown on single crystal Pt(111) and transferred to a 300 nm SiO_2 substrate on Si. Raman signatures are the same across the uniform h-BN. The inset shared between (c) and (f) shows the height distribution of AFM data from h-BN grown on polycrystalline Pt (purple) and h-BN grown on single crystal Pt(111) (blue).

Grain boundaries are visible optically in figure 3(a), corresponding to the size and shape of grains from the original metal growth substrate.

Points on different regions of the h-BN film transferred from polycrystalline Pt have different Raman signal intensities as well, which may indicate differences in film quality, coverage, and strain. This is illustrated in figure 3(b), with points 1A and 1B from the same domain showing very similar signals that both differ from points 2A and 2B in an adjacent domain. The characteristic E′ Raman peak of h-BN monolayer can be observed around 1370 cm^{-1}, and although there are small variations in its location, the peak still falls within the reported range for a monolayer [29]. The additional peak at $\sim$1460 cm^{-1} is due to the Si substrate [24, 36]. By extracting the full width at half maximum (FWHM) values from Lorentzian fits of the Raman data, we also see that the average

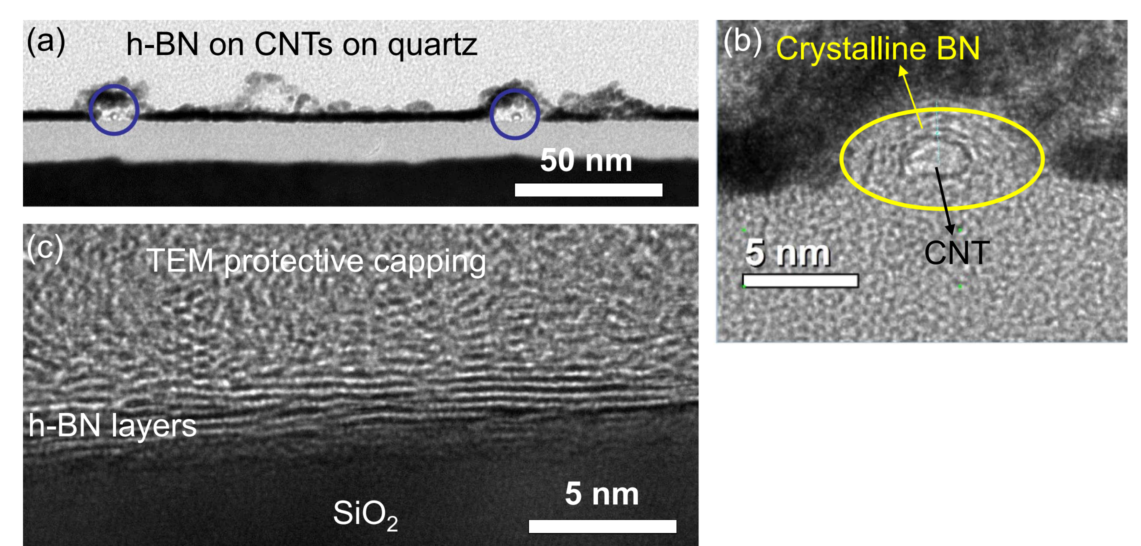

Figure 4. Cross sectional TEM images of crystalline, continuous multilayer h-BN grown by CVD on (a) single walled carbon nanotubes, with an image zoomed-in on one h-BN wrapped CNT in (b), and h-BN grown on (c) copper foil (but transferred to SiO_2 for imaging).

FWHM from grain 1 is approximately 18.6 cm^{-1}, whereas it is 16.9 cm^{-1} in grain 2. These FWHM values have been correlated with the in-plane grain size of the h-BN film, and therefore are evidence of spatial differences in film properties that may arise from different growth substrate grains [37].

The h-BN Raman peaks from different grains in figure 3(b) are also slightly shifted in wavenumber with respect to each other. This variation is common for h-BN monolayers and may be indicative of differing amounts of strain in the different grains of the film. Strain levels <1% can shift the peak by 1–2 cm^{-1}, which explains the observed variations in the monolayer measurements [29]. Small tears in the film can be seen in the AFM image in figure 3(c) with the underlying SiO_2 exposed beneath, and the measured root-mean-square (rms) surface roughness on the surface of the h-BN film is 1.70 nm. We additionally confirm the presence of monolayer h-BN grown on the polycrystalline Pt foil by measuring an approximately 4 Å step height on the edge of the film in the AFM image in supplementary information figure S4.

Figures 3(d)–(f) show optical, Raman, and AFM images of the h-BN transferred from the single crystal Pt(111) substrate; no grain boundaries are optically visible, but a scratch made in the film provides contrast against the underlying SiO_2 substrate. The AFM image in figure 3(f) has an rms surface roughness of 0.80 nm, which is lower than the film from the polycrystalline Pt even though identical transfer methods were used for each film. While surface roughness is an extrinsic measurement that is dependent on AFM scan size, resolution, scan speed, tip sharpness, and other factors, by using the same conditions for each scan we are able to compare the h-BN films from different growth substrates and conclude that the film from the Pt(111) substrate is smoother.

In the inset shared between figures 3(c) and (f), we plot the height distributions of the AFM data for the h-BN films. The h-BN film deposited on the Pt(111) substrate shows a narrower distribution than the one from the polycrystalline Pt substrate, which supports the assertion that the h-BN film is smoother when grown on a single crystal substrate. Raman spectra plotted in figure 3(e) are taken at two different points and have very similar intensities and FWHM values, indicating that the film quality and coverage are much more spatially consistent across the film. While these qualities are desirable for certain applications, a scalable process may be limited by the high cost of the single crystal Pt substrate. However, recent work has shown that large area (111) Pt can be synthesized by a cost-effective method, therefore demonstrating a potential pathway forward [38]. We are also able to reuse the Pt(111) for numerous growths that do not measurably consume the substrate material.

Next, we turn to multilayer h-BN films grown on CNTs/quartz and on Cu foil. In figure 4(a), the aligned, single-walled CNTs were grown on a quartz substrate and subsequently placed into the h-BN furnace without transfer [39]. From the TEM cross-section in figure 4(a), it is evident that h-BN selectively deposits onto each individual CNT, but not on the quartz substrate between them. This is also clear in figure 4(b), which shows a cross-sectional TEM of just one CNT that is conformally blanketed with few-layer h-BN. We can refer back to figure 1(e) for a schematic illustration of this geometry. Capping CNTs with h-BN is appealing for improving the electrical performance of CNT transistors; the lack of dangling bonds and surface charge traps make h-BN a promising candidate for higher performance devices (e.g. as gate dielectric), as has been shown with

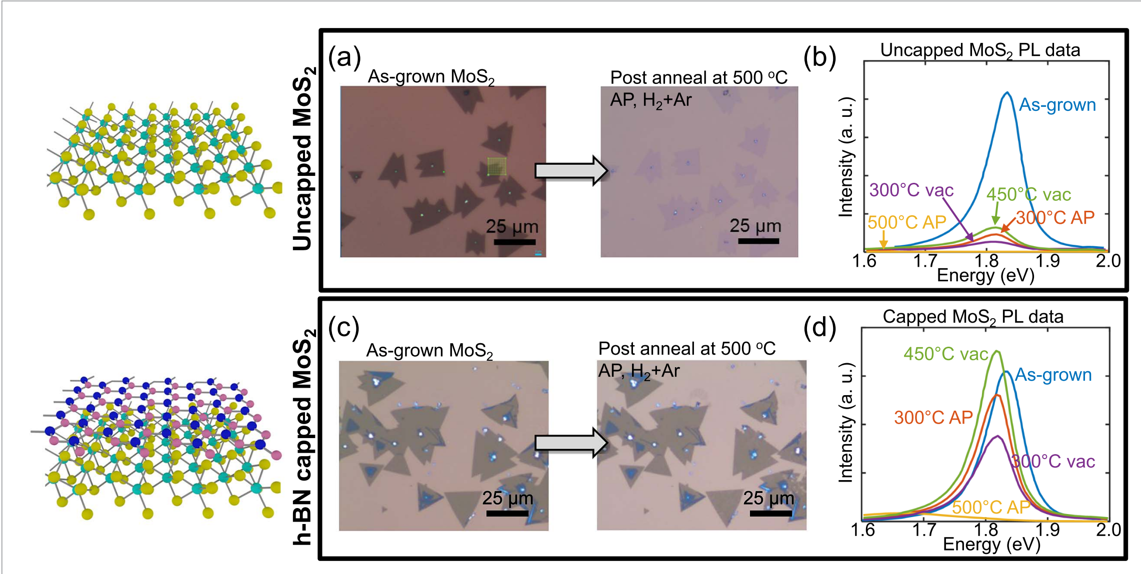

Figure 5. Optical and photoluminescence (PL) data on bare vs. h-BN capped MoS_2 exposed to elevated temperature conditions. (a) Optical images showing uncapped MoS_2 on SiO_2 before and after a 500 °C anneal at atmospheric pressure (AP) with H_2 and Ar, (b) photoluminescence data for as-grown, uncapped MoS_2 and MoS_2 films after anneals under vacuum (vac) and atmospheric pressure (AP) conditions (c) Optical images of h-BN capped MoS_2 before and after anneal, and (d) photoluminescence data of the h-BN capped MoS_2 after the same anneals.

graphene in the past [12, 40]. However, if the h-BN is grown on a different substrate and then transferred to the CNTs, residue left from the transfer process may degrade the transistor performance. Direct growth of h-BN on CNTs is a scalable method of deposition that avoids issues caused by the transfer process. We fabricate and measure the electrical properties of two-terminal CNT devices in supplementary information section E and figure S5. With the present h-BN growth, we find some (partial) current degradation in h-BN-covered CNTs, which could be averted with further deposition improvements, and by avoiding h-BN under the CNT metal contacts.

Finally, in figure 4(c), we show the cross-sectional TEM image of multilayer h-BN that has been transferred to SiO_2 from Cu for characterization purposes. These ordered layers in figure 4(c) are uniform across the image, demonstrating the spatial conformity of the deposited h-BN layers. In addition to depositing multilayers as opposed to monolayers with Pt, the h-BN on Cu may be used without transfer in specific applications, as the Cu substrate has a lower cost than Pt and therefore does not need to be reused for growths.

4. Applications

Using the films discussed above, we demonstrate the use of monolayer h-BN from the polycrystalline Pt as an encapsulation to protect monolayer MoS_2 from anneals at atmospheric pressure under 200 sccm H_2 and 200 sccm Ar flow up to 500 °C. Figure 5 shows optical images and photoluminescence (PL) spectra for MoS_2, as grown and after annealing. The MoS_2 is grown on SiO_2 on Si using CVD [41], and in figure 5(a) immediately undergoes an anneal at atmospheric pressure in a H_2/Ar environment at 500 °C; the optical images showing the film before and after clearly illustrate film degradation from the high-temperature environment. Degradation of MoS_2 films exposed to elevated temperatures in a hydrogen atmosphere has been previously shown [42, 43] and our PL results confirm this phenomenon. Figure 5(b) shows PL spectra from MoS_2 films that are annealed under different conditions, and there is significant quenching of the PL peak even down to anneals at 300 °C, indicating damage to the film. On the other hand, by transferring a monolayer of h-BN to blanket the MoS_2 prior to the anneal, the MoS_2 film is protected from degradation, as shown optically in figure 5(c). In figure 5(d), the PL spectra are retained for anneals up to 450 °C, as further evidence that the MoS_2 is protected.

In comparison, similar results have been previously achieved with encapsulation by depositing ∼15 nm Al_2O_3 onto the MoS_2 [44]. In other words, the results shown in figure 5 of this work demonstrate an h-BN capping monolayer with similar film protection performance that is only one atomic layer thick—nearly 50 times thinner than the Al_2O_3 capping layer previously used. Oxidation prevention methods are a widely researched area, and h-BN is emerging as an extremely thin candidate that can sustain high temperatures while contributing minimal weight to components [45].

To further explore applications of h-BN, we summarize other potential uses in figure 6. As schematically represented in figure 6(a), h-BN may serve as the

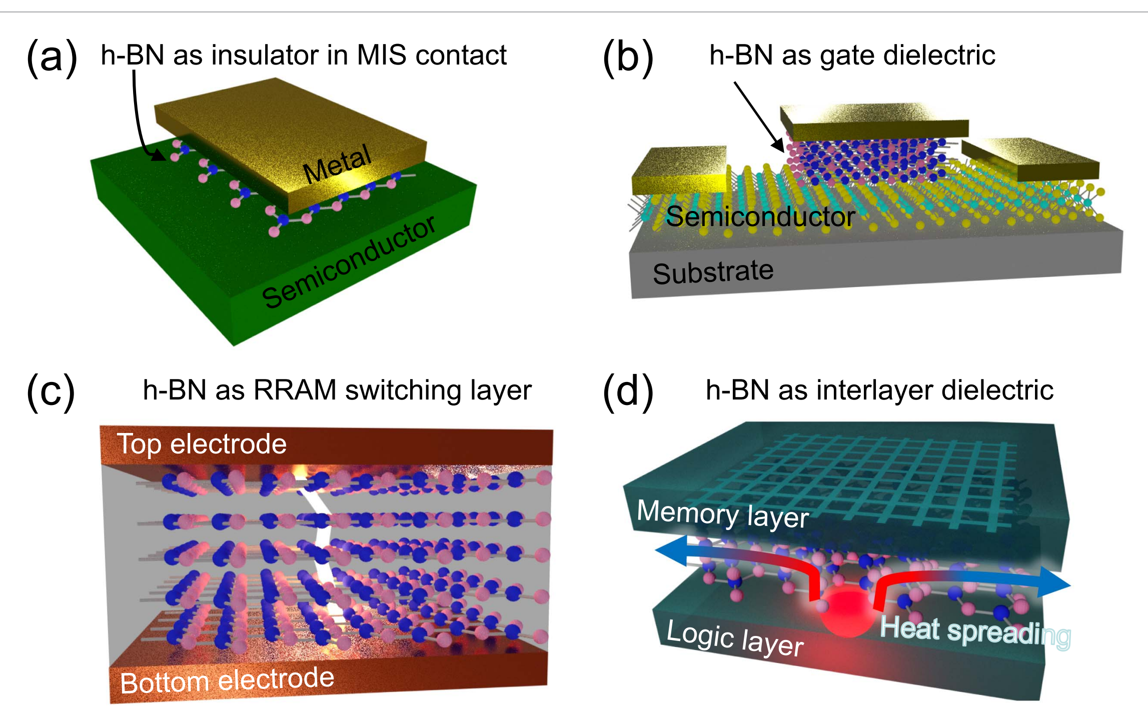

Figure 6. Examples of h-BN applications: (a) insulating layer in metal–insulator–semiconductor (MIS) contacts, (b) gate dielectric material in a transistor, (c) switching layer in RRAM devices, and (d) interlayer dielectric material with anisotropic thermal conductivity in a 3D integrated circuit (IC) to dissipate heat from a hot spot in the computing (logic) layer.

insulating layer in a metal–insulator–semiconductor (MIS) contact, depinning the Fermi level while acting as a solid-state barrier that prevents metal contacts from reacting with the semiconductor material. This concept has been experimentally demonstrated with both MoS_2 and $MoTe_2$ as the 2D semiconductor material [46, 47]. Along these lines, the h-BN lattice structure is highly impermeable to many small chemical species, and therefore is a useful solid-state barrier to prevent undesirable chemical reactions and preserve materials of interest [48]. With excellent measured dielectric properties, it has also been demonstrated as an ultrathin gate dielectric material for transistors, opening a new potential avenue to explore in the field of transistor scaling [11, 12, 49–51]. This is schematically represented in figure 6(b).

With figure 6(c), we illustrate how multilayer h-BN grown on Cu foil can be used as the switching layer of a resistive random-access memory (RRAM) device, with defects utilized to form the conductive filament [52, 53]. Finally, the high in-plane thermal conductivity of h-BN makes it a promising candidate for heat spreading applications where an electrical insulator is required [15]. Because electrical and thermal conductivity are often positively correlated (e.g. for metals), materials with a high thermal conductivity that are electrical insulators are relatively rare (e.g. diamond, BN, and AlN) [54]. In addition to this unique property, h-BN also has an anisotropic thermal conductivity between the in-plane vs. cross-plane directions, with a much lower cross-plane thermal conductivity [55]. This would make it valuable in applications where directional heat spreading is important. For example, figure 5(d) shows h-BN as the interlayer dielectric material for a three-dimensional (3D) integrated circuit, stacking a memory layer on top of a logic layer. The h-BN can spread heat laterally, and reduce peak hot spot temperatures from logic devices, while blocking the heat from affecting the memory layer above.

5. Conclusions

We have demonstrated a scalable method for depositing large-area h-BN films on various substrates (including single-crystal Pt, polycrystalline Pt and Cu, and single-wall CNTs) and characterized the resulting films. The crystallinity of the substrates affects the properties of the h-BN as well as the resulting thickness of the film, and this knowledge can be used to selectively tailor the resulting h-BN film properties. In addition, direct growth on CNT and Cu substrates can enable use of the h-BN without a transfer being necessary. We also discuss applications for h-BN grown by CVD and use this material as an ultrathin barrier layer to effectively protect a monolayer of MoS_2, allowing it to reach temperatures above the threshold at which it would typically degrade without sustaining measurable damage. This illustrates promising applications for h-BN as a protective coating against oxidation, which would be of use

in numerous industries. While future work remains needed to reduce the growth temperature of h-BN and improve the transfer process when required, this study explores h-BN synthesis and specifies potential target applications that would utilize the carefully tuned properties of the films.

Data availability statement

The data that support the findings of this study are available upon reasonable request from the authors.

Acknowledgments

This work was performed at the Stanford Nanofabrication Facility (SNF) and Stanford Nano Shared Facilities (SNSF) supported by the National Science Foundation (NSF) under award ECCS-1542152. This work was supported in part by the Air Force Office of Scientific Research (AFOSR) grants FA9550-14-1-0251 and FA9550-16-1-0126, the NSF EFRI 2-DARE grant 1542883, and the Stanford SystemX Alliance. The Pt single-crystal growth substrate and DG-G's involvement were supported by the Department of Energy, Office of Science, Basic Energy Sciences, Materials Sciences and Engineering Division, under Contract DE-AC02-76SF00515. V C acknowledges support from the Stanford Graduate Fellowship (SGF). E P acknowledges partial support from ASCENT, one of six centers in JUMP, a SRC program sponsored by DARPA.

Conflict of interest

The authors declare no competing financial interests.

ORCID iDs

Victoria Chen https://orcid.org/0000-0001-7737-2281
Joel Martis https://orcid.org/0000-0002-1580-439X
Ze Zhang https://orcid.org/0000-0002-3019-0138
David Goldhaber-Gordon https://orcid.org/0000-0001-8549-0560
Eric Pop https://orcid.org/0000-0003-0436-8534

References

[1] Pease R S 1952 An x-ray study of boron nitride *Acta Crystallogr.* **5** 356–61
[2] Cassabois G, Valvin P and Gil B 2016 Hexagonal boron nitride is an indirect bandgap semiconductor *Nat. Photon.* **10** 262–6
[3] Watanabe K, Taniguchi T and Kanda H 2004 Direct-bandgap properties and evidence for ultraviolet lasing of hexagonal boron nitride single crystal *Nat. Mater.* **3** 404–9
[4] Song L *et al* 2010 Large scale growth and characterization of atomic hexagonal boron nitride layers *Nano Lett.* **10** 3209–15
[5] Sichel E K, Miller R E, Abrahams M S and Buiocchi C J 1976 Heat capacity and thermal conductivity of hexagonal pyrolytic boron nitride *Phys. Rev.* B **13** 4607–11
[6] Paszkowicz W, Pelka J B, Knapp M, Szyszko T and Podsiadlo S 2002 Lattice parameters and anisotropic thermal expansion of hexagonal boron nitride in the 10–297.5 K temperature range *Appl. Phys.* A **75** 431–5
[7] Mortazavi B, Pereira L F C, Jiang J-W and Rabczuk T 2015 Modelling heat conduction in polycrystalline hexagonal boron-nitride films *Sci. Rep.* **5** 13228
[8] Alam M T, Bresnehan M S, Robinson J A and Haque M A 2014 Thermal conductivity of ultra-thin chemical vapor deposited hexagonal boron nitride films *Appl. Phys. Lett.* **104** 013113
[9] Jo I, Pettes M T, Kim J, Watanabe K, Taniguchi T, Yao Z and Shi L 2013 Thermal conductivity and phonon transport in suspended few-layer hexagonal boron nitride *Nano Lett.* **13** 550–4
[10] Wang C, Guo J, Dong L, Aiyiti A, Xu X and Li B 2016 Superior thermal conductivity in suspended bilayer hexagonal boron nitride *Sci. Rep.* **6** 25334
[11] Roy T, Tosun M, Kang J S, Sachid A B, Desai S B, Hettick M, Hu C C and Javey A 2014 Field-effect transistors built from all two-dimensional material components *ACS Nano* **8** 6259–64
[12] Yamoah M A, Yang W, Pop E and Goldhaber-Gordon D 2017 High-velocity saturation in graphene encapsulated by hexagonal boron nitride *ACS Nano* **11** 9914–9
[13] Sinha S, Takabayashi Y, Shinohara H and Kitaura R 2016 Simple fabrication of air-stable black phosphorus heterostructures with large-area hBN sheets grown by chemical vapor deposition method *2D Mater.* **3** 035010
[14] Jeong Y, Douglas O, Misra U, Tanjil M R-E, Watanabe K, Taniguchi T and Wang M C 2021 Mitigation of electromigration in metal interconnects via hexagonal boron nitride as an Ångström-thin passivation layer *Adv. Electron. Mater.* **7** 2100002
[15] Choi D, Poudel N, Park S, Akinwande D, Cronin S B, Watanabe K, Taniguchi T, Yao Z and Shi L 2018 Large reduction of hot spot temperature in graphene electronic devices with heat-spreading hexagonal boron nitride *ACS Appl. Mater. Interfaces* **10** 11101–7
[16] Song X *et al* 2015 Chemical vapor deposition growth of large-scale hexagonal boron nitride with controllable orientation *Nano Res.* **8** 3164–76
[17] Park J-H *et al* 2014 Large-area monolayer hexagonal boron nitride on Pt foil *ACS Nano* **8** 8520–8
[18] Kim G, Jang A-R, Jeong H Y, Lee Z, Kang D J and Shin H S 2013 Growth of high-crystalline, single-layer hexagonal boron nitride on recyclable platinum foil *Nano Lett.* **13** 1834–9
[19] Kim K K *et al* 2012 Synthesis of monolayer hexagonal boron nitride on Cu foil using chemical vapor deposition *Nano Lett.* **12** 161–6
[20] Shi Y *et al* 2010 Synthesis of few-layer hexagonal boron nitride thin film by chemical vapor deposition *Nano Lett.* **10** 4134–9
[21] Chen T-A *et al* 2020 Wafer-scale single-crystal hexagonal boron nitride monolayers on Cu (111) *Nature* **579** 219–23
[22] Lee J S *et al* 2018 Wafer-scale single-crystal hexagonal boron nitride film via self-collimated grain formation *Science* **362** 817–21
[23] Behura S, Nguyen P, Che S, Debbarma R and Berry V 2015 Large-area, transfer-free, oxide-assisted synthesis of hexagonal boron nitride films and their heterostructures with MoS_2 and WS_2 *J. Am. Chem. Soc.* **137** 13060–5
[24] Behura S, Nguyen P, Debbarma R, Che S, Seacrist M R and Berry V 2017 Chemical interaction-guided, metal-free growth of large-area hexagonal boron nitride on silicon-based substrates *ACS Nano* **11** 4985–94
[25] Sprenger J K, Sun H, Cavanagh A S, Roshko A, Blanchard P T and George S M 2018 Electron-enhanced atomic layer deposition of boron nitride thin films at room temperature and 100 °C *J. Phys. Chem.* C **122** 9455–64
[26] Hui F, Fang W, Leong W S, Kpulun T, Wang H, Yang H Y, Villena M A, Harris G, Kong J and Lanza M 2017 Electrical

homogeneity of large-area chemical vapor deposited multilayer hexagonal boron nitride sheets *ACS Appl. Mater. Interfaces* **9** 39895–900
[27] Xiang R I *et al* 2020 One-dimensional van der Waals heterostructures *Science* **367** 537–42
[28] Baitalow F, Baumann J, Wolf G, Jaenicke-Rößler K and Leitner G 2002 Thermal decomposition of B–N–H compounds investigated by using combined thermoanalytical methods *Thermochim. Acta* **391** 159–68
[29] Gorbachev R V *et al* 2011 Hunting for monolayer boron nitride: optical and Raman signatures *Small* **7** 465–8
[30] Arenal R, Ferrari A C, Reich S, Wirtz L, Mevellec J-Y, Lefrant S, Rubio A and Loiseau A 2006 Raman spectroscopy of single-wall boron nitride nanotubes *Nano Lett.* **6** 1812–6
[31] Paffett M T, Simonson R J, Papin P and Paine R T 1990 Borazine adsorption and decomposition at Pt(111) and Ru(001) surfaces *Surf. Sci.* **232** 286–96
[32] Preobrajenski A B, Vinogradov A S, Ng M L, Ćavar E, Westerström R, Mikkelsen A, Lundgren E and Mårtensson N 2007 Influence of chemical interaction at the lattice-mismatched h−BN/Rh(111) and h−BN/Pt(111) interfaces on the overlayer morphology *Phys. Rev.* B **75** 245412
[33] Gao Y, Ren W, Ma T, Liu Z, Zhang Y, Liu W-B, Ma L-P, Ma X and Cheng H-M 2013 Repeated and controlled growth of monolayer, bilayer and few-layer hexagonal boron nitride on Pt foils *ACS Nano* **7** 5199–206
[34] Mullins W W 1957 Theory of thermal grooving *J. Appl. Phys.* **28** 333–9
[35] Gao L *et al* 2012 Repeated growth and bubbling transfer of graphene with millimetre-size single-crystal grains using platinum *Nat. Commun.* **3** 699
[36] Zwick A and Carles R 1993 Multiple-order Raman scattering in crystalline and amorphous silicon *Phys. Rev.* B **48** 6024–32
[37] Nemanich R J, Solin S A and Martin R M 1981 Light scattering study of boron nitride microcrystals *Phys. Rev.* B **23** 6348–56
[38] Jin S *et al* 2018 Colossal grain growth yields single-crystal metal foils by contact-free annealing *Science* **362** 1021–5
[39] Patil N, Lin A, Myers E R, Ryu K, Badmaev A, Zhou C, Wong H-S P and Mitra S 2009 Wafer-scale growth and transfer of aligned single-walled carbon nanotubes *IEEE Trans. Nanotechnol.* **8** 498–504
[40] Dean C R *et al* 2010 Boron nitride substrates for high-quality graphene electronics *Nat. Nanotechnol.* **5** 722–6
[41] Smithe K K H *et al* 2017 Intrinsic electrical transport and performance projections of synthetic monolayer MoS_2 devices *2D Mater.* **4** 011009
[42] Ye G, Gong Y, Lin J, Li B, He Y, Pantelides S T, Zhou W, Vajtai R and Ajayan P M 2016 Defects engineered monolayer MoS_2 for improved hydrogen evolution reaction *Nano Lett.* **16** 1097–103
[43] Liu K-K *et al* 2012 Growth of large-area and highly crystalline MoS_2 thin layers on insulating substrates *Nano Lett.* **12** 1538–44
[44] Yalon E *et al* 2017 Energy dissipation in monolayer MoS_2 electronics *Nano Lett.* **17** 3429–33
[45] Liu Z *et al* 2013 Ultrathin high-temperature oxidation-resistant coatings of hexagonal boron nitride *Nat. Commun.* **4** 2541
[46] Cui X *et al* 2017 Low-temperature ohmic contact to monolayer MoS_2 by van der Waals bonded Co/h-BN electrodes *Nano Lett.* **17** 4781–6
[47] Mleczko M J *et al* 2019 Contact engineering high-performance n-type $MoTe_2$ transistors *Nano Lett.* **19** 6352–62
[48] Gallagher P, Lee M, Petach T A, Stanwyck S W, Williams J R, Watanabe K, Taniguchi T and Goldhaber-Gordon D 2015 A high-mobility electronic system at an electrolyte-gated oxide surface *Nat. Commun.* **6** 6437
[49] Kim K K, Hsu A, Jia X, Kim S M, Shi Y, Dresselhaus M, Palacios T and Kong J 2012 Synthesis and characterization of hexagonal boron nitride film as a dielectric layer for graphene devices *ACS Nano* **6** 8583–90
[50] Jang S K, Youn J, Song Y J and Lee S 2016 Synthesis and characterization of hexagonal boron nitride as a gate dielectric *Sci. Rep.* **6** 30449
[51] Lee G-H *et al* 2015 Highly stable, dual-gated MoS_2 transistors encapsulated by hexagonal boron nitride with gate-controllable contact, resistance, and threshold voltage *ACS Nano* **9** 7019–26
[52] Shi Y *et al* 2018 Electronic synapses made of layered two-dimensional materials *Nat. Electron.* **1** 458–65
[53] Wang C-H *et al* 2018 3D monolithic stacked 1T1R cells using monolayer MoS_2 FET and hBN RRAM fabricated at low (150 °C) temperature *IEEE Int. Electron Devices Meeting (IEDM)* (*San Francisco, CA*) pp 22.5.1–4
[54] Xu R L *et al* 2019 Thermal conductivity of crystalline AlN and the influence of atomic-scale defects *J. Appl. Phys.* **126** 185105
[55] Jiang P, Qian X and Yang R 2017 Time-domain thermoreflectance (TDTR) measurements of anisotropic thermal conductivity using a variable spot size approach *Rev. Sci. Instrum.* **88** 074901

SUPPLEMENTARY INFORMATION

Application-Driven Synthesis and Characterization of Hexagonal Boron Nitride Deposited on Metals and Carbon Nanotubes

Victoria Chen[1], Yong Cheol Shin[1], Evgeny Mikheev[2], Qing Lin[3], Joel Martis[4], Ze Zhang[4], Sukti Chatterjee[5], Arun Majumdar[4,6], H.-S. Philip Wong[1], David Goldhaber-Gordon[2,7], and Eric Pop[1,3,6*]

1. Department of Electrical Engineering, Stanford University, Stanford CA 94305, USA
2. Department of Physics, Stanford University, Stanford CA 94305, USA
3. Department of Materials Science & Engineering, Stanford University, Stanford, CA 94305, USA
4. Department of Mechanical Engineering, Stanford University, Stanford CA 94305, USA
5. Applied Materials, Inc., Santa Clara, CA 95054, United States
6. Stanford Precourt Institute for Energy, Stanford, CA, 94305, USA
7. Stanford Institute for Materials & Energy Sciences, SLAC Natl. Accelerator Lab, Menlo Park, CA, USA

* Contact: epop@stanford.edu

A. Transfer Process

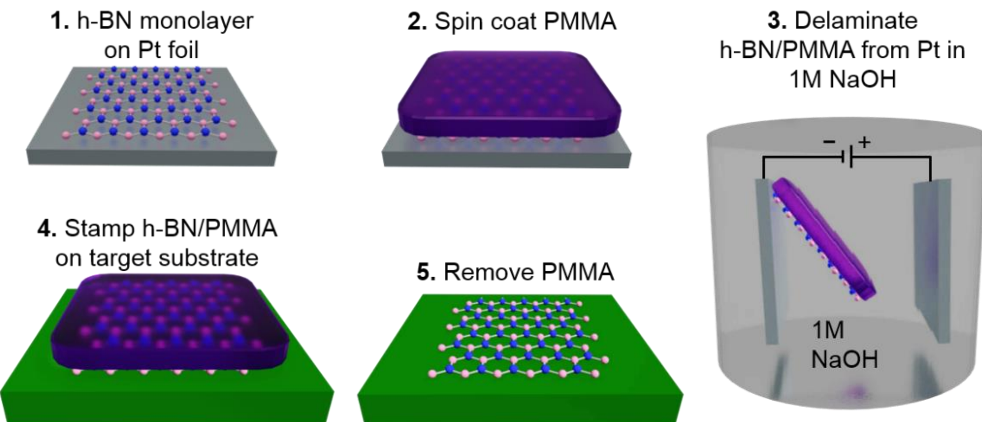

Figure S1. Schematic of transfer process illustrating the delamination of monolayer h-BN deposited onto Pt foil and transferred to the target substrate.

In order to transfer the h-BN monolayer films from the Pt growth substrates for characterization and comparison, we utilize an electrochemical bubbling-based transfer method that has been previously demonstrated [1, 2], as shown in figure S1. After the h-BN is grown on the Pt foil, a 200 nm layer of PMMA is spun onto it and baked at 80°C on a hotplate for 30 min. Then, this stack is subsequently placed in a 1M solution of NaOH and attached to the negative terminal of a power supply, with another Pt foil as the positive electrode. Applying a voltage will generate bubbling at the interface of the h-BN and Pt, allowing the monolayer h-BN capped with the PMMA scaffold to peel off the Pt surface. Once the h-BN/PMMA stack is removed, it is subsequently rinsed in deionized (DI) water and then placed onto the target substrate. Immediately after, a nitrogen spray gun is aimed perpendicular to the sample surface, and the gentle gas flow is used to flatten the film and remove trapped air bubbles. The PMMA is then removed by soaking the sample in acetone for 30 minutes. This relatively clean transfer process allows for the continued reuse of expensive Pt foil substrates, as it does not require any etching and so can preserve the substrate and h-BN films.

B. Orientation Mapping

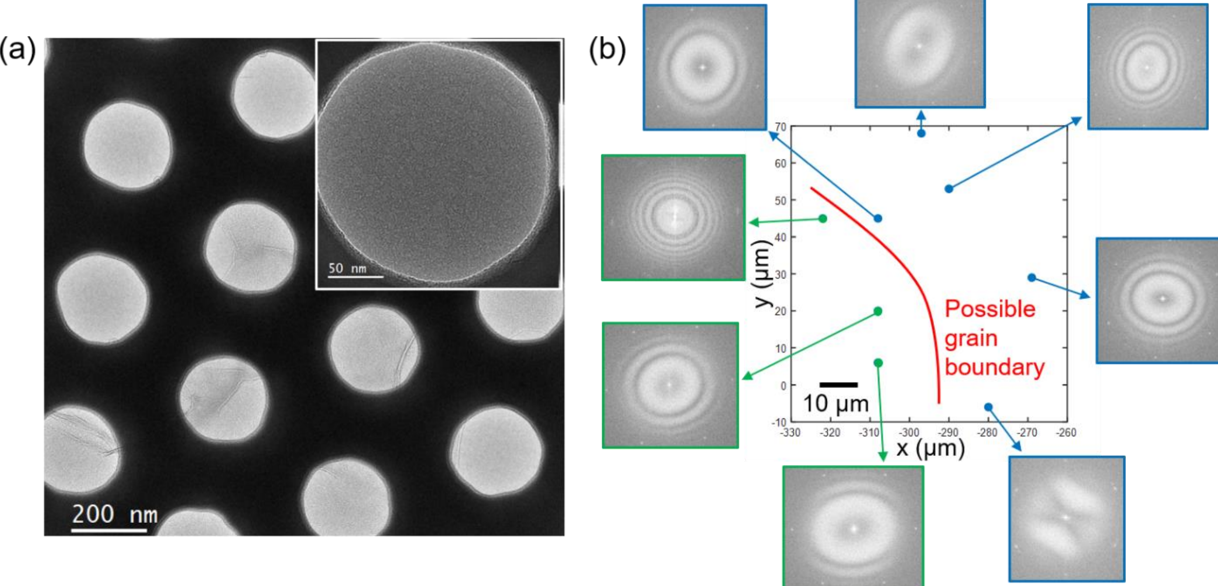

Figure S2. TEM images showing diffraction patterns of monolayer h-BN transferred from polycrystalline Pt to a SiN grid. (a) SiN grid with partial coverage of monolayer h-BN (inset showing zoomed-in image of one SiN hole) and (b) spatially mapped diffraction patterns showing similar h-BN orientations in regions of comparable size to the polycrystalline Pt substrate grain sizes.

For TEM imaging, we transfer monolayer h-BN grown on the polycrystalline Pt foil onto a SiN grid, and this grid is pictured in figure S2(a). Then, by examining the diffraction patterns of the h-BN at different points spaced apart from each other in figure S2(b), we observe two distinct clusters of points with two different orientations – one group of points is marked in blue and consistently shows the same orientation in spots up to ~80 μm apart, while the green points mark an adjacent region with a different orientation. A possible grain boundary between the two distinct orientations is sketched with a red line in figure S2(b), and the size of the regions is comparable to the grain size of the polycrystalline Pt growth substrate. Although the number of points imaged was limited due to imperfect h-BN film transfer to these delicate SiN grids, the measured clusters of similar orientations supports the hypothesis that the polycrystalline Pt grain size is a limiting factor in the h-BN domain size.

The singular sets of diffraction spots in figure S2(b) also serve as evidence that there cannot be multiple h-BN layers stacked in an AB orientation. While this does not definitively prove the presence of monolayer h-BN on its own (as there could be more than one layer still if they follow an AA' stacking order), it is further indication that the film is most likely a monolayer, an assertion also supported through other characterization techniques.

C. AFM of Polycrystalline Pt Grain Boundary

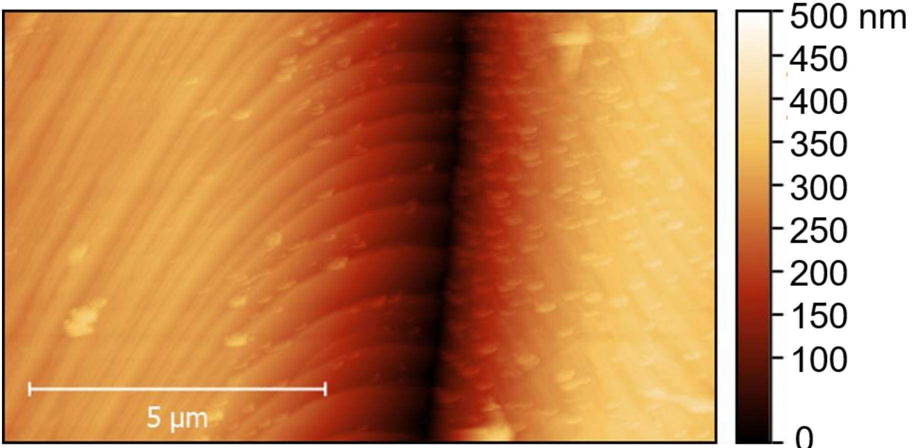

Figure S3. AFM topography scan over a grain boundary in the polycrystalline Pt substrate, illustrating the thermal grooving (~250 nm deep) occurring in the Pt.

The AFM topography image in figure S3 maps the surface of the polycrystalline Pt at a grain boundary and shows evidence of thermal grooving. This occurs due to Pt atom migration at the high temperature and low pressure growth conditions, and is typically unavoidable for polycrystalline metals [3]. These relatively deep grooves contribute to the spatial non-homogeneity of h-BN deposited on the polycrystalline Pt and may be avoided through the use of single crystal metal growth substrates.

D. AFM Step Height Measurement

In addition to measuring an h-BN Raman peak location consistent with a monolayer film [main text figures 3(b,e)], we also use AFM to consider the topography near the edge of an h-BN film transferred from polycrystalline Pt to SiO_2. The measured step height is ~4 Å, which also indicates that the film is just one layer thick. We note there is roughness on the surface due to polymer residue from the transfer process, and we account for this roughness in estimating the h-BN step height.

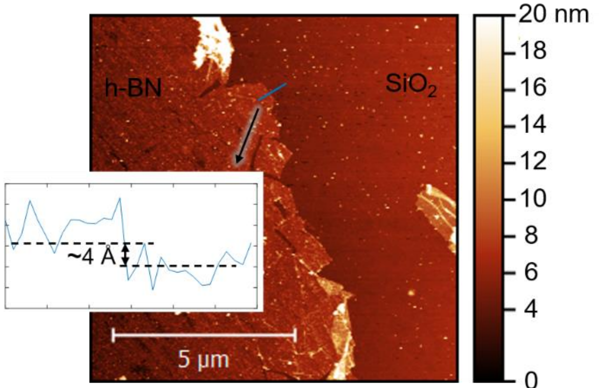

Figure S4. AFM topography image with inset line profile measuring the step height of the monolayer h-BN transferred to SiO_2. The roughness on the surface of the h-BN and SiO_2 surface is due to residue from the transfer process.

E. CNT Electrical Data

To further characterize the deposition of h-BN on carbon nanotubes (CNTs), we fabricate two-terminal CNT devices directly on their quartz growth substrates, with evaporated Ti/Pt contacts [4]. Each device has between 5 and 10 aligned CNTs between their electrical contacts, which are 1 μm apart. These CNTs were kept on their original growth substrate (quartz) to ensure that they would be pristine for the electrical tests, and not influenced by any transfer process or residue. We made two types of devices, 7 devices with h-BN deposited on top and 10 control devices without, as shown in figure S5(a).

The plot in figure S5(a) shows that the CNT devices suffer some (partial) current degradation after the h-BN deposition, and the inset schematics illustrate the device structures. However, we find this current decrease is due to two main factors: the added contact resistance from the h-BN layers under the contacts and CNT oxidation from O_2 leakage into our furnace at high temperatures. The former issue is difficult to avoid here, as it would require etching the h-BN (under the contacts) without damaging the CNTs. The second issue, however, is more specific to our particular furnace setup and could be avoided with better, industrial furnaces.

To confirm the suspected O_2 leakage issue, we also performed several control measurements on similar CNT devices annealed at high temperatures *without* the use of the ammonia borane precursor. In other words, this replicated the temperatures and H_2/Ar gases the CNTs are exposed to during our h-BN growth process, except without the h-BN growth. The results in figure S5(b) show that current degradation in these CNT devices occurs after they were exposed to furnace temperatures above 600°C, without the presence of any BN chemistry, which is due to oxygen and moisture entering the furnace chamber when it is pumped down to typical growth pressure (~900 mTorr) [5]. Although this effect is unavoidable in our specific academic CVD tool, the furnace chambers typically used for industrial applications have a much lower leak rate (~1 mTorr/min. or lower) [6]. Therefore, our demonstration of direct h-BN deposition onto CNTs could remain a viable technique for capping CNTs without the need for a transfer process, as long as the furnace leak rate can be mitigated.

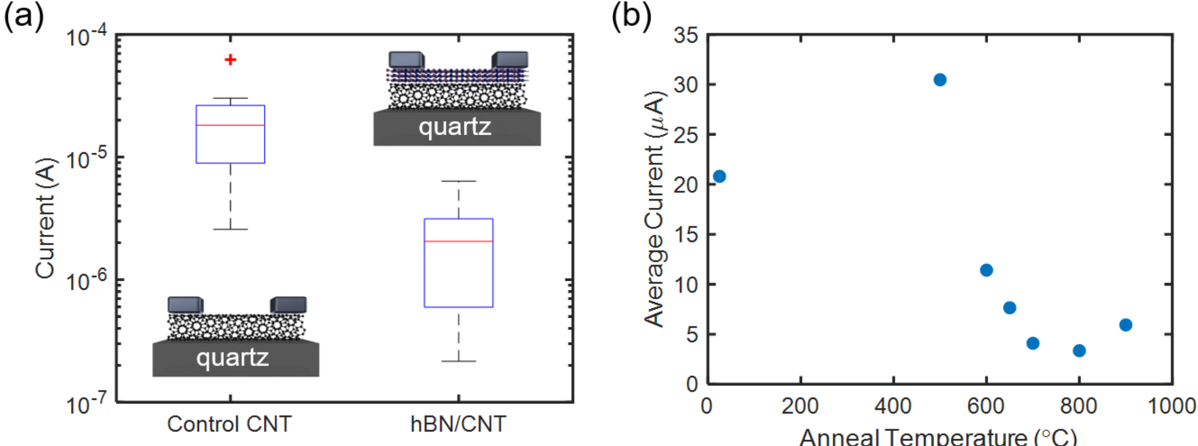

Figure S5. Electrical data showing (a) current degradation from 10 control CNT devices to 7 CNT devices after h-BN deposition (insets schematically illustrating the device structures) and (b) average current across CNTs after annealing at high temperatures without any precursor material, ensuring the lack of h-BN chemistry. This control experiment reveals that CNT current degradation occurs due to (unwanted) oxygen leakage into our furnace, not due to the h-BN growth chemistry.

Supplementary References

1. Gao, L., et al., *Repeated growth and bubbling transfer of graphene with millimetre-size single-crystal grains using platinum.* Nat Commun, 2012. **3**: p. 699.
2. Kim, G., et al., *Growth of high-crystalline, single-layer hexagonal boron nitride on recyclable platinum foil.* Nano Lett, 2013. **13**(4): p. 1834-9.
3. Mullins, W.W., *Theory of Thermal Grooving.* Journal of Applied Physics, 1957. **28**(3): p. 333-339.
4. Patil, N., et al., *Wafer-Scale Growth and Transfer of Aligned Single-Walled Carbon Nanotubes.* IEEE Transactions on Nanotechnology, 2009. **8**(4): p. 498-504.
5. Hata, K., et al., *Water-Assisted Highly Efficient Synthesis of Impurity-Free Single-Walled Carbon Nanotubes.* Science, 2004. **306**: p. 1362-1364.
6. Enicks, D. and G. Oleszek, *Vacuum science considerations for rapid reactor recovery with extremely low oxygen in low temperature low pressure chemical vapor deposition of $Si_{1-x}Ge_x$ and $Si_{1-x-y}Ge_xC_y$ films.* Journal of Vacuum Science & Technology A: Vacuum, Surfaces, and Films, 2006. **24**(3): p. 467-473.